Energy 254 (2022) 124366

Contents lists available at ScienceDirect

Energy

journal homepage: www.elsevier.com/locate/energy

Thermo-electro-hydraulic analysis of jet impingement bifacial photovoltaic thermal (JIBPVT) solar air collector

Win Eng Ewe [a, **], Ahmad Fudholi [a, b, *], Kamaruzzaman Sopian [a], Refat Moshery [c], Nilofar Asim [a], Wahidin Nuriana [d], Adnan Ibrahim [a]

[a] Solar Energy Research Institute, Universiti Kebangsaan Malaysia, 43600, Bangi, Selangor, Malaysia
[b] Research Center for Energy Conversion and Conservation, National Research and Innovation Agency (BRIN), Indonesia
[c] SEGI University, Malaysia
[d] Department of Mechanical Engineering, Faculty of Engineering, Merdeka University of Madiun, East Java, Indonesia

ARTICLE INFO

Article history:
Received 25 July 2021
Received in revised form
19 April 2022
Accepted 22 May 2022
Available online 24 May 2022

Keywords:
Bifacial solar cell
Photovoltaic thermal collectors
Jet impingement
Heat transfer
Thermohydraulic
Electrohydraulic

ABSTRACT

The effects of impinging air jet on the thermo-electro-hydraulic performance of a bifacial PVT with different packing factors are entirely unclear. Here, we have proposed a dual-functional jet plate reflectors are introduced to induce jet air cooling and increase the light absorption at the rear part of the bifacial PV module. The effects of jet plate reflectors with different configurations on the system's performance are investigated and studied. The simulation results were verified and validated with the experimental findings. Increasing the distance between jet holes reduces the interference and enhances the heat transfer, which led to higher friction and greater pumping power. Net energy gain is the key to calculate hydraulic efficiency, by subtracting the pumping power from the energy output. Therefore, the system's best performance can be explained by the lowest Re to generate max efficiencies. Jet impingement bifacial photovoltaic thermal (JIBPVT) with 36 jet-holes has the greatest jet spacing between the jet holes and optimum performance. The maximum thermal energy gain and electrical energy produced were achieved at lower critical values of Re, which are 9929 and 5667, respectively. JIBPVT has the optimum thermal, electro, and thermo-electro-hydraulic efficiencies, with 57.3%, 10.36%, and 83.93%, respectively.

1. Introduction

Because of human activity, the value of natural resources such as fossil fuels for power production has increased dramatically during the past decade [1–3]. Compared to rural regions, the urban population's share of the overall population is increasing at an alarming rate. According to national statistics, about 30% of the world's population lived in cities in 1950, with that number expected to rise to 66% by 2050 [4]. Thus, the community's growth will boost the need for new structures, both residential and non-residential. As a consequence of growth, a slew of environmental issues has come to the forefront. In addition, environmental problems have arisen due to industrialization, including air pollution [5]. Clean, long-lasting electricity from renewable sources such as solar energy can be generated instead of fossil fuels to conserve energy and reduce the negative impact of the building industry on global warming and climate change. Renewable energy sources, such as solar energy, can be used in place of fossil fuels to conserve energy and reduce the negative impact of the building industry on global warming and climate change [6].

Flat plate solar air collectors (SACs) are the most widely used solar collectors due to their simple construction and high efficiency [7]. The thermal performance of the SAC, on the other hand, is inferior owing to the limited thermal conductivity and heat capacity of the material. Hence, incorporation of a SAC with air flowing between the top and lower sections of the absorber plate as part of the collector's design [8].

In the year 1991, the first glazed jet impingement solar air collector was developed [9]; employing a jet air impingement mechanism may improve the maximum thermal efficiency of a flat plate

* Corresponding author. Solar Energy Research Institute, Universiti Kebangsaan Malaysia, 43600, Bangi, Selangor, Malaysia.
** Corresponding author.
E-mail addresses: p97455@siswa.ukm.edu.my (W.E. Ewe), a.fudholi@ukm.edu.my (A. Fudholi).

https://doi.org/10.1016/j.energy.2022.124366
0360-5442/

SAC by up to 26.5%. According to the study's findings [10], the thermal efficiency of the unglazed jet impingement solar collector is 21% greater than the thermal efficiency of the conventional flat plate solar collector (SAC). Likewise, The relationship between the friction factor and the Nusselt number for jet plate SAC has been investigated in jet diameter, spanwise, streamwise, and Reynolds number for jet plate SAC [11]. When these features are combined with conventional design, the authors found that they contribute the most to a 3.5 increase in friction factor and a 2.6 increase in heat transfer rate, respectively. Another study conducted by the same authors showed that the optimum jet plate characteristics might be theoretically calculated by finding the greatest thermohydraulic efficiency and using the correlations discussed in the previous study [12]. The optimum design configuration is then found for the spanwise pitch, jet diameter, and streamwise pitch ratios of 0.065, 0.435, and 0.865, respectively, for the three parameters of spanwise pitch, jet diameter, and streamwise pitch ratio [13]. Comparative analysis was carried out on the thermal efficiency of flat-plate SACs and perforated plates with low porosity [14]. It seems that the low porosity perforated plate outperformed the flat plate SAC by up to 23%, according to the findings. It was discovered that the addition of a single flow dual air channel SAC with jet impingement increased the overall thermal and exergy efficiency of a single flow single air channel SAC with jet impingement by 21.2% and 22.4%, respectively, when compared to when the SAC was used alone [15].

Photovoltaic thermal (PVT) systems are hybrid systems that integrate thermal and photovoltaic systems to produce electrical and thermal energy simultaneously in a single installation [16]. The performance of the solar panel, on the other hand, would deteriorate as the temperature increases. A variety of cooling methods must be used as a consequence in order to improve energy production by decreasing the temperature of the panel [17]. The performance of PVT with the jet plate was evaluated using analytical modeling [18], and the results revealed a 54% total efficiency. By impinging Si−C nanofluids on a jet array [19], it has been shown that the overall efficiency of a PVT solar collector may be improved. The efficiencies of 12.8% for electrical efficiency, 85% for thermal efficiency, and 97.8% for overall efficiency have been shown in tests. In a subsequent study [20], the same authors repeated their findings with the PVT with water jet, which resulted in a total efficiency of 81%.

To increase the area for solar radiation absorption, a bifacial PV module was used with the aid of a reflector [21]. In Ref. [22], an investigation of double-pass bifacial PVT air collector with mirror reflectors was done by using parallel air flow for cooling. Moreover, a bifacial PVT air collector with semi-mirror reflector was investigated in Ref. [23] by using similar cooling method, which led to a maximum total energy efficiency of about 67%. However, due to the very thin boundary layer formed by jet impingement over the heated absorber plate, jet impingement further improves the convective heat transfer coefficient than parallel airflows [24]. Jet impingement has been shown to be very effective in a number of engineering and industrial applications. Nevertheless, the jet impingement mechanism is always associated with poor hydraulic design, resulting in dead zone flow or high fan motor power [25]. Based on the literature, there is insufficient study on the cooling of bifacial PVT systems with jet air impingement.

The objectives of the current work are introducing a novel design of bifacial PVT with jet impingement and a dual-functional jet plate reflectors with different geometric configurations (such as jet holes, jet spanwise and streamwise pitch ratios). The jet plate reflectors were used as a reflector to reflect the incident light onto the rear part of bifacial PV module, and product jet air cooling to the rear part, simultaneously.

2. Design and simulation

2.1. Description of JIBPVT solar air collector

The schematic cross-sectional view of JIBPVT solar air collector is given in Fig. 1 and Fig. 2, along with airflow and light transmission direction, respectively. Three components make up the collector: a bifacial photovoltaic panel, a jet plate reflector, and an insulated backplate. Additionally, this system utilizes two channels: (i) an air channel between the bifacial photovoltaic panel and the jet plate reflector; and (ii) an air channel between the jet plate reflector and the backplate. Referring to Fig. 1, air from the surrounding area will initially enter the lower channel before passing through the perforations in the jet plate reflector and entering the top channel. The air exits the upper channel at a high rate of speed and collides with the bottom portion of the bifacial photovoltaic panel. Heat transmission occurs here between the bifacial photovoltaic panel and the surrounding air. The proposed design has a dimension of 0.703 m length, 0.684 m width, and 0.12 m height. The depth of each air channel is 0.025 m. The investigation is carried out on a bifacial photovoltaic panel with packing factors of 0.22, 0.33, and 0.66 with a mass flow rate of 0.014−0.035 kg/s.

2.2. Design of holes on jet plate reflector

This study proposes using a jet plate reflector to improve cooling and light absorption on the backside of a bifacial photovoltaic panel. The hole pattern on the jet plate reflector is determined by the dimensions and placement of the PV cells in a real-world bifacial PV panel. Figs. 3−5 illustrate three distinct jet plate reflectors, each with a distinct streamwise pitch X = 0.09 m, 0.105 m, and 0.126 m; a unique spanwise pitch Y = 0.081 m, 0.0945 m, and 0.1134 m; and a unique variety of holes N = 64, 49, and 36. The thickness of the jet plate reflector is set to 0.001 m, while the width of each jet hole is set to 0.003 m. Table 1 summarises the variables and fixed design and operation characteristics.

2.3. Energy balance of JIBPVT solar air collector

A one-dimensional heat flow analytical model in steady-state is created to determine the energy balance between each component of the system. Fig. 6 illustrates the heat transfer coefficients at each component of the system. In addition, energy analysis was performed to determine the thermal, panel, and total energy efficiency. The following assumptions were made for the bifacial PVT model to ease the analytical analysis:

i) Forced convection heat transmission occurs along the channels.
ii) The convection heat transfer coefficient is equal and constant between the air heater components and the air along the flow channel.
iii) Temperature drops are insignificant through the absorber plate, jet plate, and backplate.
iv) PV cells are considered to have the same temperature throughout the PV panel.
v) The front and rear PV cells on the bifacial panel have identical electrical efficiency.
vi) No leakage occurs in the airflow routes.
vii) The air mass flow rate in channels 1 and 2 is identical, $\dot{m}_1 = \dot{m}_2$.
viii) For long-wavelength light, the sky is regarded to be a black body.
ix) Thermal losses at the collector's edge are insignificant.

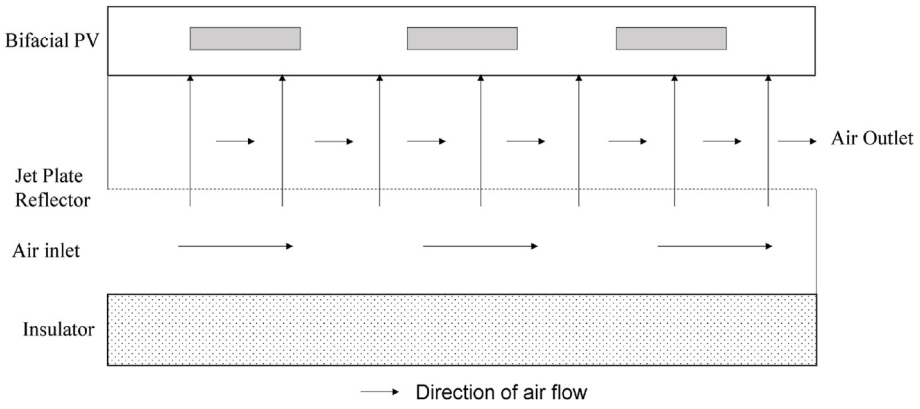

Fig. 1. The direction of airflow of JIBPVT.

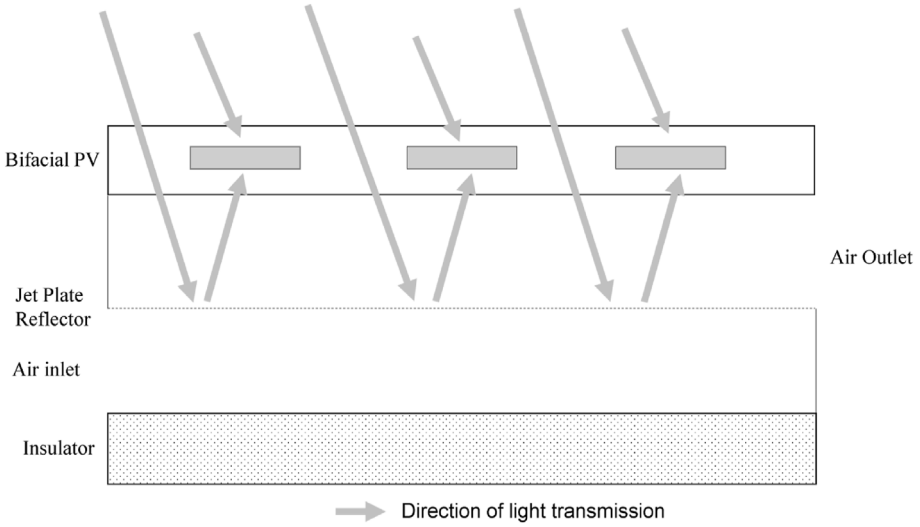

Fig. 2. The direction of light transmission of JIBPVT.

x) The internal energy variation of each component of the studied PVT collector is neglected.
xi) The heat losses by conduction is neglected.

The equations for each component of the system's energy balance are listed. The left-hand sides of the equations represent the heat gained or absorbed from solar radiation or other collector components, while the right-hand sides represent the heat dissipated or lost at each collector component.

Energy Balance Equations (Gain Energy = Loss Energy):

i) PV laminate:

$$I_{pv} = U_t(T_{pv} - T_a) + h_{rpvj}(T_{pv} - T_j) + h_{cpvf2}\left(T_{pv} - T_{f2}\right) \quad 2.3.1$$

ii) Air flow bet. PV and jet plate, f2:

$$h_{cpvf2}\left(T_{pv} - T_{f2}\right) + h_{cjf2}\left(T_j - T_{f2}\right) = 2\dot{m}\mathbb{C}_p\left(T_{f2} - T_{f2i}\right) \Big/ WL \quad 2.3.2$$

iii) Jet plate reflector:

$$I_j + h_{rpvj}(T_{pv} - T_j) = h_{rjb}(T_j - T_b) + h_{cjf1}\left(T_j - T_{f1}\right) + h_{cjf2}\left(T_j - T_{f2}\right) \quad 2.3.3$$

iv) Air flow bet. jet plate and back plate, f1:

$$h_{cjf1}\left(T_j - T_{f1}\right) + h_{cbf1}\left(T_b - T_{f1}\right) = 2\dot{m}\mathbb{C}_p\left(T_{f1} - T_{f1i}\right) \Big/ WL \quad 2.3.4$$

v) Back plate:

$$h_{rjb}(T_j - T_b) = U_b(T_b - T_a) + h_{cbf1}\left(T_b - T_{f1}\right) \quad 2.3.5$$

In the preceding equations, $T_{f2} = (T_{f2i} + T_{f2o})/2$ and $T_{f1} = (T_{f1i} + T_{f1o})/2$ correspond to the average temperature of each channel. $T_{f2i} = T_{f1o}$ is the temperature at the jet hole. There are two types of heat transfer of the system: i) h_c, the convective heat transfer; ii) h_r, the radiative heat transfer. The useful energy gain at the channel can be written as $2\dot{m}\mathbb{C}_p(T_f - T_{fi})/(WL)$. U_t *and* U_b indicates the heat loss from the collector's top and rear to the environment.

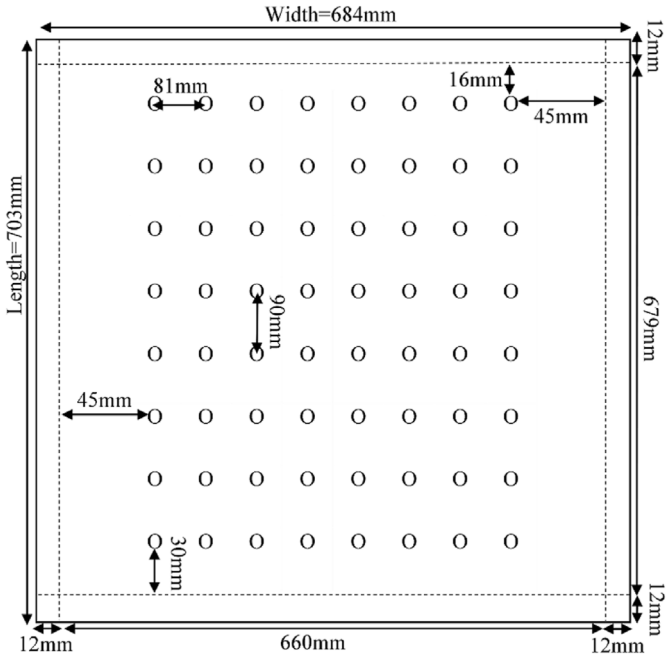

Fig. 3. Jet plate with 64 holes, X = 0.09 m and Y = 0.081 m

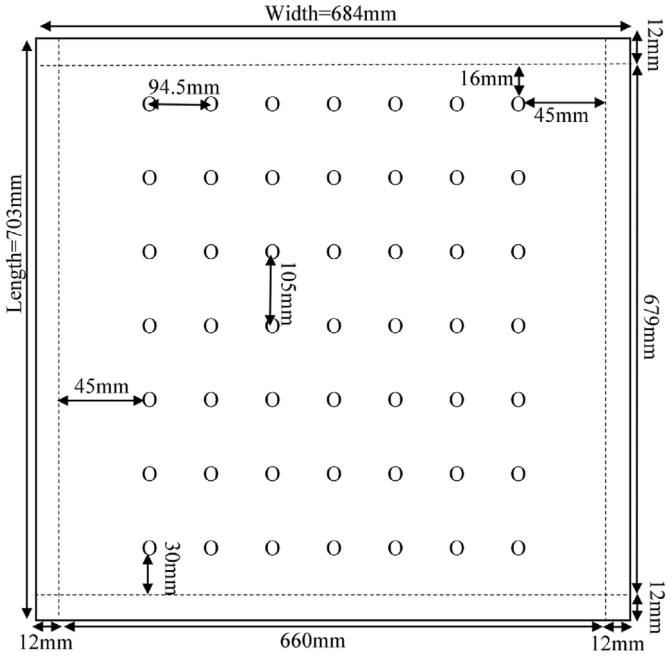

Fig. 4. Jet plate with 49 holes, X = 0.105 m & Y = 0.0945 m

The total thermal energy absorbed by the solar collector from the solar radiation splits into two parts, which are:

i) $I_j = I\tau_l(1-P)(1-n_R)$, Total heat gain by the jet plate.
ii) $I_{pv} = I_{pvfront} + I_{pvrear}$, Total heat gain by the bifacial PV panel, where $I_{pvfront}$ is the heat gain from the front bifacial PV and I_{pvrear} is the heat gain from the rear bifacial PV.

For the thermal energy received by the bifacial photovoltaic panel on the front,

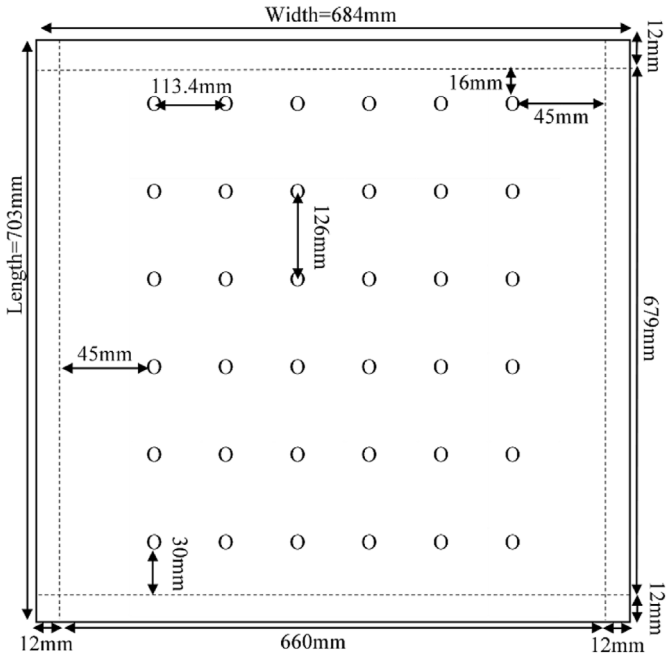

Fig. 5. Jet plate with 36 holes, X = 0.126 m and Y = 0.1134 m

Table 1
Variable and fixed design and operating parameters.

Parameters	Base values
Variable design and operating parameters	
No of PV cells	4, 6, 12
Packing factor, P	0.22, 0.33, 0.66
Number of jet holes, N	64, 49, 36
Streamwise pitch, X	0.09, 0.105, 0.126
Spanwise pitch, Y	0.081, 0.0945, 0.01134
Solar irradiance, I	700, 900 W/m^2
Air mass flow rate, $\dot{m}$	0.014–0.035 kg/s
Fixed design and operating parameters	
Length of collector, L	0.703 m
Width of collector, W	0.684 m
Height of collector, H	0.12 m
The surface area of collector, Ac	0.481 m^2
Duct depth for each channel, d	0.025 m
Absorptivity of PV cell, α_{pv}	0.91
The emissivity of PV cell, ε_{pv}	0.6
Absorptivity of lamination, α_l	0.1
The transmittance of lamination, τ_l	0.85
The emissivity of jet plate reflector, ε_j	0.11
The reflectivity of jet plate reflector, n_R	0.7
The emissivity of the backplate, ε_b	0.25
The thickness of insulation, t_{in}	0.004 m
Thermal conductivity of insulation, k_{in}	0.037 W/mK
Speed of wind, V_w	1 m/s
The temperature of the atmosphere, T_a	300 K
The temperature of inlet air, T_i	301 K
Stefan's Boltzmann constant, σ	5.67×10^{-8} W/m^2.K^4
Electrical efficiency at a reference condition, n_{ref}	0.16
Temperature coefficient	0.0045 K^{-1}
The temperature at a reference condition	298 K
The thickness of the jet plate reflector	0.001 m
Diameter of jet holes	0.003 m

$$I_{pvfront} = I\alpha_{pv}P\left(1-n_{pvfront}\right) + I\alpha_l(1-P) \quad 2.3.6$$

$I\alpha_{pv}P(1-n_{pvfront})$ is the total amount of heat absorbed by the front photovoltaic cell, solar radiation is absorbed by the photovoltaic

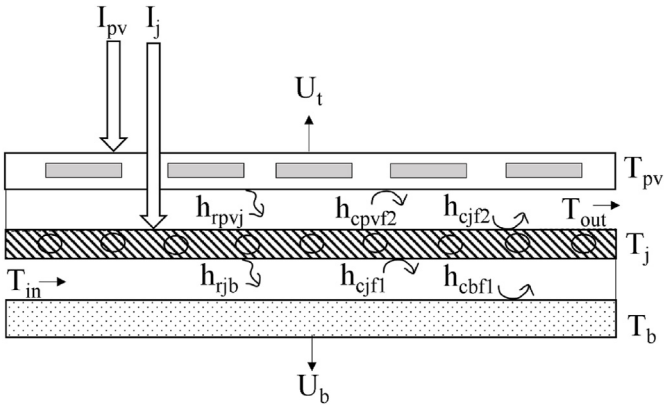

Fig. 6. Energy balance of bifacial PVT.

cell with packing factor P. $n_{pvfront}$ will convert to electricity, so $(1-n_{pvfront})$ will transfer to heat; $I\alpha_l(1-P)$ is the total heat absorbed by the front PV laminate, whereas $(1-P)$ is the area without the PV cell.

For the amount of heat absorbed by the back bifacial photovoltaic panel,

$$I_{pvrear} = I\tau_l(1-P)n_R\alpha_{pv}P(1-n_{pvrear}) + I\tau_l(1-P)n_R\alpha_l(1-P) \quad 2.3.7$$

$I\tau_l(1-P)n_R\alpha_{pv}P(1-n_{pvrear})$ is the total heat absorbed by the rear photovoltaic cell, solar radiation will travel through glass and the photovoltaic laminate with an area $(1-P)$ and will be reflected by the jet plate, and absorbed by the photovoltaic cell with a packing factor P. n_{pvrear} will transfer to electricity, so $(1-n_{pvrear})$ will transfer to heat; $I\tau_l(1-P)n_R\alpha_l(1-P)$ is the amount of heat absorbed by the back photovoltaic lamination in total.

2.4. Determination of temperature for components of JIBPVT solar air collector

The equation 2.3.1 to 2.3.5 can be reworked in matrix type 5 × 5 as follows to compute the various solar air collector part temperatures, [A][T] = [C], where [A] matrix denotes the equation with an unknown; [T] matrix represents the predicted average temperature; and [C] matrix denotes the equation with values.

$$\begin{bmatrix} A1 & -h_{cpvf2} & -h_{rpvj} & 0 & 0 \\ -h_{cpvf2} & A2 & -h_{cjf2} & 0 & 0 \\ -h_{rpvj} & -h_{cjf2} & A3 & -h_{cjf1} & -h_{rjb} \\ 0 & 0 & -h_{cjf1} & A4 & -h_{cbf1} \\ 0 & 0 & -h_{rjb} & -h_{cbf1} & A5 \end{bmatrix} \begin{bmatrix} T_{pv} \\ T_{f2} \\ T_j \\ T_{f1} \\ T_b \end{bmatrix} = \begin{bmatrix} C1 \\ C2 \\ C3 \\ C4 \\ C5 \end{bmatrix} \quad 2.4.1$$

$$A1 = U_t + h_{rpvj} + h_{cpvf2} \quad 2.4.2$$

$$A2 = h_{cpvf2} + h_{cjf2} + 2\dot{m}C_p/(WL) \quad 2.4.3$$

$$A3 = h_{rpvj} + h_{cjf1} + h_{cjf2} + h_{rjb} \quad 2.4.4$$

$$A4 = h_{cjf1} + 2\dot{m}C_p/(WL) + h_{cbf1} \quad 2.4.5$$

$$A5 = h_{rjb} + U_b + h_{cbf1} \quad 2.4.6$$

$$C1 = I_{pv} + U_tT_a \quad 2.4.7$$

$$C2 = 2\dot{m}C_pT_{f2i}/(WL) \quad 2.4.8$$

$$C3 = I_j \quad 2.4.9$$

$$C4 = 2\dot{m}C_pT_{f1i}/(WL) \quad 2.4.10$$

$$C5 = U_bT_a \quad 2.4.11$$

The mean temperature vectors in equation 2.4.1 can be determined using the matrix inversion approach $[T] = [A]^{-1}[C]$, which was developed in MATLAB.

2.5. Heat transfer coefficients

For top loss coefficient: U_t is given by:

$$U_t = \frac{1}{(h_w + h_{rpvs})^{-1}} \quad 2.5.1$$

where convective heat transfer of wind, h_w is given by:

$$h_w = 5.7 \times 3.8(V_w) \quad 2.5.2$$

and radiative heat transfer coefficient from PV panel to the sky, h_{rpvs} is given by Ref. [26]:

$$h_{rpvs} = \sigma\varepsilon_{pv}(T_{pv}+T_s)\left(T_{pv}^2 + T_s^2\right)(T_{pv}-T_s) \Big/ (T_{pv}-T_a) \quad 2.5.3$$

and temperature of sky, T_s is given by:

$$T_s = 0.0552\left(T_a^{1.5}\right) \quad 2.5.4$$

For radiative heat transfer coefficient between PV panel, jet plate reflector, and backplate, h_{rpvj} and h_{rjb} is given by:

$$h_{rpvj} = \sigma(T_{pv}+T_j)\left(T_{pv}^2 + T_j^2\right) \Big/ \left(\frac{1}{\varepsilon_{pv}} + \frac{1}{\varepsilon_j} - 1\right) \quad 2.5.5$$

$$h_{rjb} = \sigma(T_j+T_b)\left(T_j^2 + T_b^2\right) \Big/ \left(\frac{1}{\varepsilon_j} + \frac{1}{\varepsilon_b} - 1\right) \quad 2.5.6$$

For convective heat transfer coefficient between PV panel and airflow in the upper channel, h_{cpvf2} is given by:

$$h_{cpvf2} = k \times Nu_{pvf2}/D_h \quad 2.5.7$$

where Nusselt number, Nu_{pvf2} is given by Ref. [11]:

$$Nu_{pvf2} = \left(1.658 \times 10^{-3}\right)\left(Re_2^{0.8512}\right)\left(\frac{X}{D_h}\right)^{0.1761}\left(\frac{Y}{D_h}\right)^{0.141} \left(\frac{D_j}{D_h}\right)^{-1.9854} \times e^{\left(-0.3498\times\left(\log\left(\frac{D_j}{D_h}\right)\right)^2\right)} \quad 2.5.8$$

For convective heat transfer coefficient between jet plate reflector and airflow in upper and lower channel, h_{cjf2} & h_{cjf1} is given by Ref. [9]:

$$h_{cjf2} = \left(\frac{A_e}{A_c}\right) \times k \times Nu_{jf2} \Big/ D_h \quad 2.5.9$$

$$h_{cjf1} = \left(\frac{A_e}{A_c}\right) \times k \times Nu_{jf1} \Big/ D_h \quad 2.5.10$$

where Nusselt number, Nu_{jf2} and Nu_{jf1} is given by Ref. [15]:

$$Nu_{jf2} = 0.0293\left(Re_2{}^{0.8}\right) \quad 2.5.11$$

$$Nu_{jf1} = 0.0293\left(Re_1{}^{0.8}\right) \quad 2.5.12$$

and effective heat transfer area of the jet plate, A_e is given by:

$$A_e = A_c - N\pi D_j{}^2 + 2N_T N \quad 2.5.13$$

For convective heat transfer coefficient between backplate and airflow in the lower channel, h_{cbf1} is given by:

$$h_{cbf1} = h_{cjf1} \times \left(\frac{A_c}{A_e}\right) \quad 2.5.14$$

For the bottom lost coefficient, U_b is given by:

$$U_b = k_{in}/t_{in} \quad 2.5.15$$

For hydraulic diameter, D_h is given by:

$$D_h = \left(\frac{4Wd}{2(W+d)}\right) \quad 2.5.16$$

For Reynolds number, Re is given by:

$$Re = \frac{\dot{m}D_h}{Wd\mu} \quad 2.5.17$$

According to empirical correlations established by Ref. [27], physical qualities of air that are believed to fluctuate linearly with temperature in Kelvin is:

Specific heat capacity of air, C_p is given by:

$$C_p = 1.0057 + 0.000066(T - 300) \quad 2.5.18$$

The density of air, ρ is given by:

$$\rho = 1.1774 - 0.00359(T - 300) \quad 2.5.19$$

Thermal conductivity of air, k is given by:

$$k = 0.02624 + 0.0000758(T - 300) \quad 2.5.20$$

The viscosity of air, μ is given by:

$$\mu = [1.983 + 0.00184(T - 300)] \times 10^{-5} \quad 2.5.21$$

2.6. Energy efficiencies

For the thermal energy efficiency of the system, $n_{thermal}$ can be calculated by:

$$n_{thermal} = \frac{Qu}{(I \times A_c)} \quad 2.6.1$$

where useful heat gain, Qu can be calculated by:

$$Qu = \dot{m}C_p(T_o - T_i) \quad 2.6.2$$

For the electrical energy efficiency of the system, n_{panel} can be calculated by:

$$n_{panel} = \frac{P_{max}}{IA_c} \quad 2.6.3$$

where electrical power generated, P_{max} can be calculated by Ref. [21]:

$$P_{max} = IA_c\alpha_{pv}P\left(n_{pvfront}\right) + IA_c\tau_I(1-P)n_R\alpha_{pv}P\left(n_{pvrear}\right) \quad 2.6.4$$

and front and rear part of bifacial PV cell efficiency, $n_{pvfront}$ *and* n_{pvrear} can be calculated by Ref. [23]:

$$n_{pvfront} = n_{pvrear} = n_{ref}\left(1 - B\left(T_{pv} - T_{ref}\right)\right) \quad 2.6.5$$

For the total thermal energy efficiency, n_{total} can be calculated by Ref. [28]:

$$n_{total} = n_{thermal} + \frac{n_{panel}}{n_{powerplant}} \quad 2.6.6$$

where $n_{powerplant} = 0.38$, is the efficiency of a conventional power plant as the conversion factor for electrical energy to thermal energy.

2.7. Thermo-electro-hydraulic efficiency

Active convection heat transfer requires a fan or pump to generate airflow into a system. Although a higher mass flow rate will increase the heat transfer rate and thermal efficiency, the mechanical pumping power required to force air through the system should be considered. Hence the effective efficiency or thermo-electro-hydraulic efficiency, $n_{thermoelectro}$ can be calculated using the equations:

$$n_{thermoelectro} = n_{thermo} + \frac{n_{electro}}{n_{powerplant}} \quad 2.7.1$$

Thermohydraulic efficiency, n_{thermo} can be calculated based on net thermal energy gain, which is obtained by subtracting equivalent thermal energy that will be required to overcome the friction power penalty from the useful energy gain [29]:

$$n_{thermo} = \frac{Q_u - P_m/C_o}{IA_c} \quad 2.7.2$$

$C_o = 0.2$ is the conversion factor of mechanical energy to thermal energy, consisting of various efficiencies (efficiency of a conventional power plant, 0.38; transmission efficiency, 0.9; motor efficiency, 0.9; pump efficiency, 0.74).

For mechanical power requires to force air through the system, P_m can be calculated by Ref. [30]:

$$P_m = \frac{\dot{m} \times \Delta p}{\rho} \quad 2.7.3$$

Pressure drop appears when there are 2 points of a flowing fluid with different pressure in a channel due to friction. During the passage of fluid through a tube, pressure drops occur due to frictional forces produced by the resistance to flow acting on the fluid. The primary factors of fluid flow resistance in a pipe are the velocity of the fluid through the pipe and the fluid's viscosity. The amount of pressure loss rises in direct proportion to the total frictional shear forces present throughout the pipe network. For total pressure drop of the system, Δp is the sum of the pressure drop in the lower and

upper channels:

$$\Delta p = \Delta p1 + \Delta p2 \quad 2.7.4$$

where the pressure drop, $\Delta p1$, $\Delta p2$ can be calculated by Ref. [31]:

$$\Delta p1 = 2f_1 L G_1{}^2 \Big/ (D_h \rho); \quad 2.7.5$$

$$\Delta p2 = 2f_2 L G_2{}^2 \Big/ (D_h \rho); \quad 2.7.6$$

'In engineering, the Moody diagram is a graph in a non-dimensional form that relates the Darcy–Weisbach friction factor f_D, Reynolds number Re, and surface roughness for fully developed flow in a circular pipe. Thus, it can predict pressure drop or flow rate down such a pipe' [35]. The friction factor in this study is calculated by using corresponding relations for friction factor, given by Blassius Equation.

For friction factor for the lower ducts, f_1 can be calculated by using the equation [32]:

$$f_1 = 0.085 \times \left(Re^{-0.25}\right) \quad 2.7.7$$

For friction factor the upper ducts, f_2 can be calculated by using the equation [11]:

$$f_2 = 0.3475 \times \left(Re^{-0.5244}\right) \times \left((X/Dh)^{0.4169}\right) \times \left((Y/Dh)^{0.5321}\right) \times \left((Dj/Dh)^{-1.4848}\right) \times exp\left(-0.2210 \times \left(\ln\left(\frac{Dj}{Dh}\right)\right)^2\right) \quad 2.7.8$$

For the mass velocity of air flowing through the duct, G_1, G_2 can be calculated by the following equation:

$$G_1 = G_2 = \dot{m} / (W \times d) \quad 2.7.9$$

Same as the thermohydraulic efficiency, electrohydraulic efficiency, $n_{electro}$ can be calculated based on net electrical generated, which is obtained by subtracting fan electricity from electricity generated from the PV panel [33]:

$$n_{electro} = \frac{P_{max} - P_{fan}}{IA_c} \quad 2.7.10$$

For the fan power, P_{fan} can be calculated by the equation:

$$P_{fan} = \frac{P_m}{n_{fan} \times n_{motor} \times n_{transmission}} \quad 2.7.11$$

where efficiency of the fan, n_{fan}, the efficiency of the motor, n_{motor}, and the efficiency of transmission, $n_{transmission}$ are referenced 0.74, 0.9, and 0.9, respectively [12].

2.8. Simulation flowchart

The simulation flowchart for this analytical investigation is depicted in Fig. 7. To begin, the dimensions and attributes of P, N, I, $\dot{m}$, T (inlet and ambient temperatures), and PVT (properties of bifacial PV module and jet plate) are set as initial inputs for coding. Second, the various heat transfer coefficients stated in Equation 2.5.1 to 2.5.21 are determined before incorporating the energy balance equation 2.3.1 to 2.3.5. Thirdly, as illustrated in equation 2.4.1 to 2.4.11, the energy balance equations are transformed to matrix form. The revised temperatures for air heater components are then determined using the matrix inversion approach. The simulation loop will continue to run until the difference in temperature readings between new and old is less than 0.001. Fourthly, the loop will terminate, and the existing temperature values will be replaced with the new ones. Finally, using equation 2.6.1 to 2.7.11, we will determine the thermal, electrical, total, thermohydraulic, electrohydraulic, and thermo-electro-hydraulic efficiencies.

2.9. Experimental setup

An experiment was conducted to investigate the energy performance of JIBPVT and validate the results from the simulation. Figs. 8 and 9 illustrate the indoor experiment setup of JIBPVT and its schematic diagram. The prototype consists of a bifacial PV panel, collector body, and jet plate reflector based on the design mentioned in Fig. 1. The size of the collector is Solar simulators with six rows of a total of 48 halogen lamps are placed at the top of the testing section to provide a heat flux to resemble the solar irradiance. Each lamp has 118 mm long and supplies 500 W of heat flux. The intensity of heat flux is controlled by digital voltage controllers and measured by using a pyranometer. In addition, the entrance and exit of the collector are attached to an insulated black box or manifolds to prevent heat loss to the surrounding. The temperature measurements were obtained from different spots around the collector by using standardized 0.2 mm of K-Type thermocouples, which are connected to an ADAM Data Acquisition. At the same time, the inlet and outlet air wind speed are measured by using an anemometer. Although the focus of the study is forced convection mode, it is necessary to use a blower or fan that can handle the collector's required volume of air and heat. Finally, a DC electronic load is used to measure the I–V curve of the PV panel.

The following experiment procedure is conducted by referring to Refs. [34,35]. Initially, 16 thermocouples will be set around the collector as shown in Table 2. Then, by adjusting the voltage controller, the airspeed of the blower and the solar irradiance of the solar simulator is set. For each experiment set, the temperature from the thermocouples around the collector was collected using a data logger (in 30-s intervals) for 30 min. The data logger assisted in establishing a stable state before recording the data. Before reporting data, a stable state was established. Stable conditions were most likely achieved when no significant temperature variations occurred between subsequent inspections observed for 20 min. During the last 10 min of the experiment, the I–V curve is plotted using the electronic load. After finishing the data collection, the collector restates for 2 h to cool down before starting the following experiment with new manipulating parameters and operational conditions. The data is then analyzed using the equations from 2.5.1 to 2.6.6. As a result, the following parameters were recorded for each cycle of scanning during the experiment:

- The average temperature of the bifacial PV panel, T_p
- The average temperature of the inlet, outlet air and ambient, T_i, T_o, T_a
- The solar irradiance, I
- The mass flow rate, $\dot{m}$
- The I–V curve

2.10. Uncertainty and error analysis

The process of evaluating the uncertainty associated with a measurement result is often called uncertainty analysis or error analysis. The complete statement of a measured value should include an estimate of the confidence level associated with the value. Correctly reporting an experimental result and its

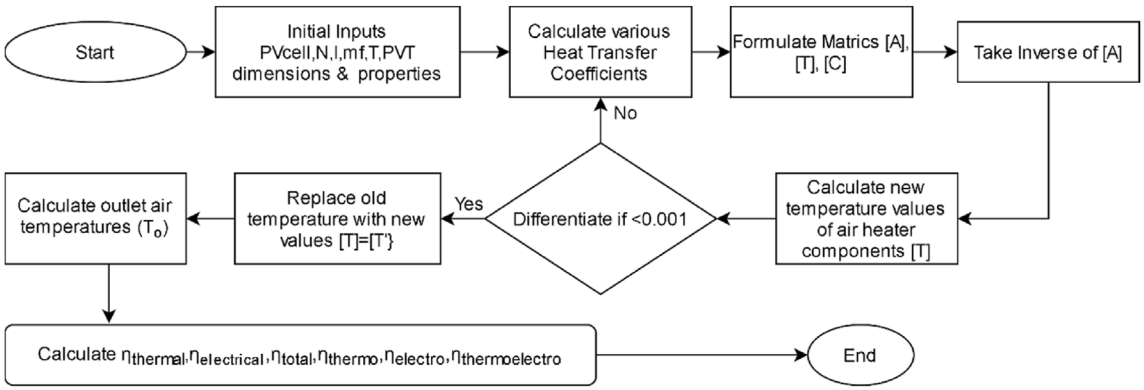

Fig. 7. Flowchart for simulation through MATLAB.

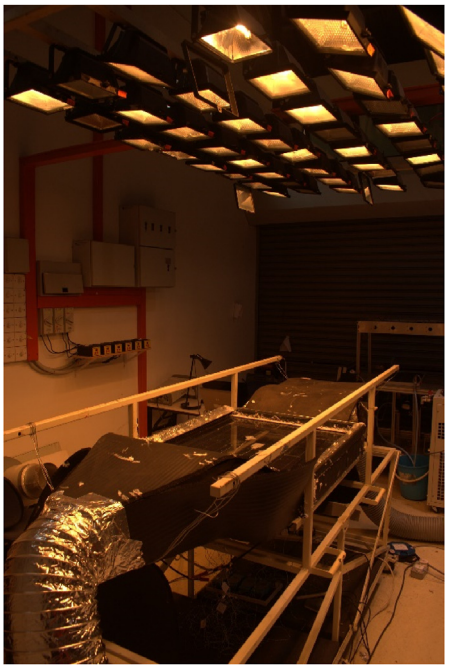

Fig. 8. Indoor experiment setup for JIBPVT.

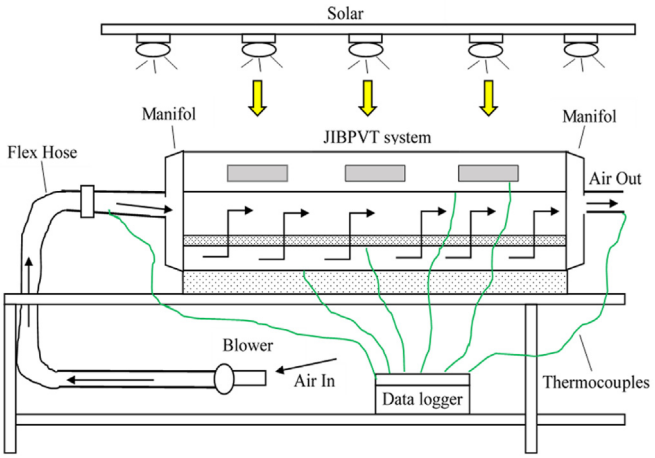

Fig. 9. Schematic of the experimental system.

Table 2
Locations of thermocouples connected to data logger.

Channel in Data Logger	Location
C1, C2, C3, C4	T_{pv}
C5, C6	T_j
C7, C8	T_b
C9, C10	T_a
C11, C12, C13	T_i
C14, C15, C16	T_o

uncertainty allows other people to make judgments about the quality of the experiment, and it facilitates meaningful comparisons with other similar values or a theoretical prediction.

Accuracy is how close a measured value is to the actual (true) value. The measurement error or absolute error is the amount of inaccuracy. The relative error is the absolute error divided by the actual measurement. The percentage error is the relative error shown as a percentage and is usually used to determine the accuracy of simulation results to the experimental results. The percentage error of a set of simulation results is calculated by:

$$\%\text{Error}=\frac{|Simulation\,results-Experimental\,results|}{Experimental\,results}=\frac{1}{N}\sum_{i=1}^{N}\frac{|\hat{X}_i-X_i|}{X_i} \quad 2.9.1$$

where $\hat{X}_i$, X_i and N are the simulation results, experimental results, and the number of experimental, respectively.

Precision is how close the measured values are to each other. Standard deviation is a measure of how spread out numbers is, which is also known as uncertainty. The standard deviation is larger when the differences are more spread. When we report the average value of N measurements, the uncertainty we should associate with this average value (relative uncertainty) is the standard deviation of the mean, often called the mean (SEM) standard error. SEM is used to determine the relative uncertainties that occurred during the measurements of parameters, which is calculated by:

$$\sigma_{\overline{X}}=\frac{\sigma}{\sqrt{N}}=\frac{\sqrt{\frac{1}{N-1}\sum_{i=1}^{N}\frac{|\overline{X_i}-X_i|}{X_i}}}{\sqrt{N}}=\sqrt{\frac{1}{N(N-1)}\sum_{i=1}^{N}\frac{|\overline{X_i}-X_i|}{X_i}} \quad 2.9.2$$

where σ, $\overline{X_i}$, X_i and N are the standard deviation, mean measured results, measured results, and the number of measured results, respectively.

Instrument selection, condition, calibration, surroundings, observation, reading, and test planning can lead to errors and

uncertainties. For example, the current experiment used appropriate sensors to evaluate temperatures, solar radiation, and air velocity. Table 3 summarises the uncertainty associated with parameter measurements. In our situation, the standard deviation of the mean, generally referred to as "Type An Uncertainty," is generated from a statistical analysis of the reported measurements taken at each location during the collector's steady-state operation [36,37].

3. Results and discussions

Graphical representations are utilized to investigate the link between hydraulic efficiency and various design and operating characteristics, as indicated in Table 1. Validation of simulation results with experimental results is carried out to ensure the accuracy. In order to carry out a comprehensive study on thermo-electro-hydraulic efficiencies, the analytical investigation is chosen for data analysis due to the limitation of the experimental work. The mass flow rate of the experimental study is insufficient to investigate the performance of the proposed system in turbulent regions. Hence, the range of air mass flow rate is extended to 0.01–0.2 kg/s. The optimum operating parameters are used to obtain the optimum results (P = 0.66 and I = 900 W/m^2).

3.1. Model validation

Model validation aims to analyze the model's precision through past data for which we already have actual results. The simulation algorithm built-in MATLAB for assessing the efficiency of JIBPVT was validated by comparing it to the experiment results. The simulation results are validated with the experimental results by calculating the percentage errors to determine the accuracy of simulation results. Table 4 and Fig. 10 show a comparison of simulation and experimental results for thermohydraulic and electrohydraulic efficiency of JIBPVT at different mass flow rate and solar irradiance. JIBPVT with 12 cells bifacial PV panel and 36 holes jet plate reflector was chosen for the comparison. A high degree of agreement between the simulation and experiment results due to the high accuracy shown in the comparison. The average accuracy percentages of simulation results for thermo and electrohydraulic efficiency are 94.62% and 98.48%, respectively.

The simulation results have higher thermohydraulic efficiency than experimental results due to higher thermal energy output as no leakage issues was assumed in simulation. However, higher thermal energy output will lead to bifacial PV panel operates at higher temperature and induced lower electricity generation. Hence, the simulation results have less eletrohydraulic efficiency than experimental results.

3.2. Friction factor and pressure drop

Reynolds number is used instead of mass flow rate to study the flow characteristics of air. Fig. 11 illustrates the relation of mass flow rate and Reynolds number. A straight line is shown in the graph, which means that the Re is highly correlated to $\dot{m}$. Refers to Ref. [27], laminar flow region is located at Re < 2300; the transition flow region is located at 2300<Re < 6000; the turbulent flow region is located at Re > 6000.

Friction factor and pressure drop at the upper channel between the PV panel and jet plate is plotted against Re in Fig. 12. A decreasing trend is shown for the friction factor from the figure, while vice versa for the pressure drop. As expected, the friction factor will drop with increased Re, according to the Moody diagram. This is because friction causes pressure to decrease when air flows through a channel, resulting in the pressure at the exit being consistently lower than the pressure at the intake, where pressure drop exists. According to Bernoulli's principle, an increase in a fluid's speed coincides with decreased static pressure or decreased fluid's potential energy. Besides, jet air at higher Re will increase the airflow turbulence and result in higher friction. Hence, the greater the speed at which fluid flows through a pumped system, the greater the pressure loss. Overall, higher Re induced lower friction factor and higher pressure drop.

A comparison is made between the different jet plate reflectors with different N, X, and Y. Jet plate reflector with 36 holes has the highest friction factor and pressure drop throughout the Re. An increase in jet spacing (X and Y) between the jet holes will decrease jet interference, increasing the airflow turbulence and leading to higher friction. As a result, increasing in jet spacing will increase the friction factor and pressure drop. The friction factor and pressure drop are in the range of 0.2 to 0.03 and 1.3–144.45 Pa, when Re increases from 1409 to 28404. The highest friction factors of JIBPVT with 36, 49 and 64 jet-holes are 0.205, 0.172 and 0.149, while the lowest friction factors are 0.042, 0.036 and 0.031, respectively. The highest pressure drops of JIBPVT with 36, 49 and 64 jet-holes are 144.48, 121.50, and 104.96, while the lowest pressure drop are 1.792, 1.507, and 1.301, respectively.

3.3. Net energy gain and pumping power

Fig. 13 shows the thermal energy gain and pumping power versus Re for JIBPVT with 36 jet holes at 900 W/m^2. Higher air velocity will increase the system's heat transfer and thermal gain and induce higher frictional losses, as mentioned above. Hence, greater pumping power is needed to overcome the friction to generate higher air velocity in a channel. A net thermal gain is identified in the figure by calculating the difference between the thermal energy gain and pumping power. The net thermal gain reaches its highest at Re = 9929, in which the maximum thermal gain at minimum pumping power is achieved. The respective maximum thermal gain and pumping power are 258.31 W and 10.33 W, respectively.

Fig. 14 represents the electrical energy generated and fan power versus Re for JIBPVT with 36 jet holes at 900 W/m^2. Higher air velocity will increase the cooling effect of the system and enhance the PV performance, which results in higher electrical energy generation. Based on the explanation above, the fan power increases with higher air velocity. The net electrical generated is

Table 3
Relative uncertainty during measurements of the parameters.

Parameters	Unit	Uncertainty comment or margin of error
Ambient air temperature	$^\circ C$	$\pm 0.07 \leq \sigma_{\overline{X}} \leq \pm 0.29$
Collector inlet temperature	$^\circ C$	$\pm 0.02 \leq \sigma_{\overline{X}} \leq \pm 0.10$
Collector outlet temperature	$^\circ C$	$\pm 0.04 \leq \sigma_{\overline{X}} \leq \pm 0.16$
Air velocity	m/s	$\pm 0.02 \leq \sigma_{\overline{X}} \leq \pm 0.05$
Solar intensity	W/m^2	$\pm 0.29 \leq \sigma_{\overline{X}} \leq \pm 1.45$

Table 4
Comparison of simulation and experimental results for thermohydraulic and electrohydraulic efficiency of JIBPVT.

$\dot{m}$ (kg/s)	I (W/m^2)	n_{thermo}			$n_{electro}$			Accuracy %	
		Model	Exp.	% Error	Model	Exp.	% Error	n_{thermo}	$n_{electro}$
0.014	700	40.74	38.05	7.07	10.20	10.21	0.13	92.93	99.87
	900	41.61	40.25	3.39	9.84	9.88	0.40	96.61	99.60
0.016	700	42.51	39.76	6.93	10.27	10.34	0.67	93.07	99.33
	900	43.43	41.22	5.34	9.93	10.04	1.03	94.66	98.97
0.018	700	44.04	41.06	7.25	10.32	10.46	1.34	92.75	98.66
	900	44.98	42.36	6.18	10.01	10.26	2.38	93.82	97.62
0.025	700	47.95	45.48	5.41	10.46	10.65	1.81	94.59	98.19
	900	49.03	46.51	5.42	10.21	10.42	2.06	94.58	97.94
0.035	700	51.33	49.49	3.71	10.52	10.77	2.35	96.29	97.65
	900	52.57	50.99	3.11	10.34	10.66	3.03	96.89	96.97
Avg				5.38			1.52	94.62	98.48

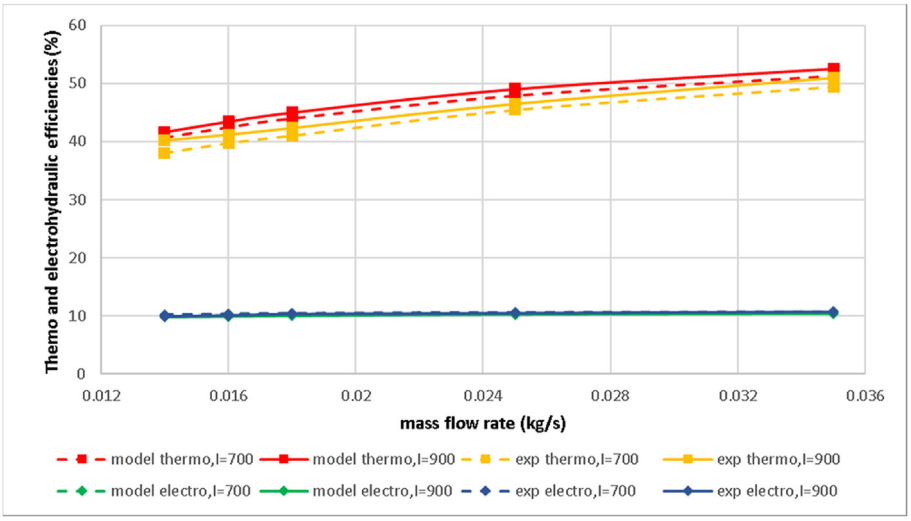

Fig. 10. Comparison of simulation results with experimental results of JIBPVT.

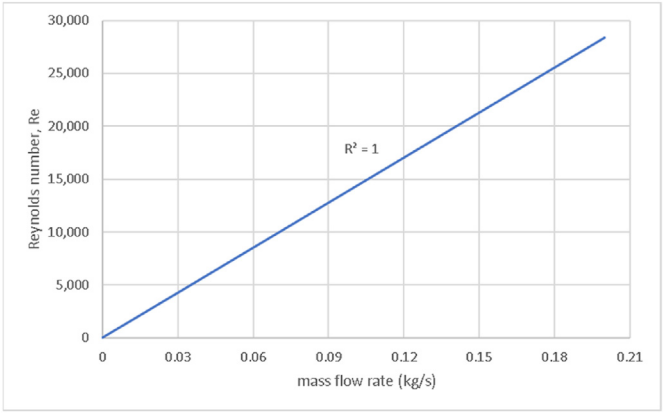

Fig. 11. Reynolds number versus mass flow rate.

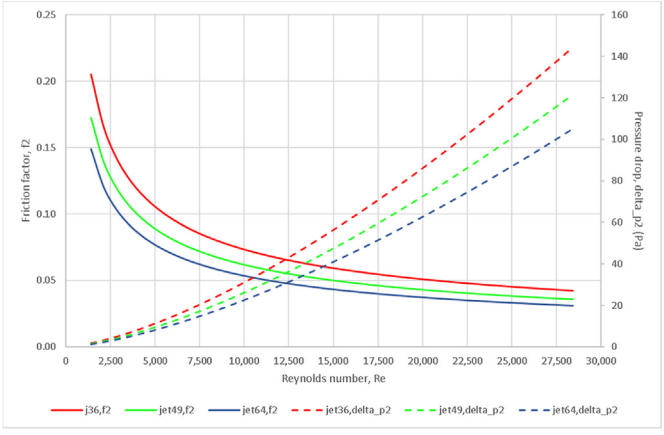

Fig. 12. Friction factor and pressure drop versus Re

shown in the figure by deducting the fan power from the electrical energy generated. The net electrical generated reaches its highest at Re = 5667. The respective electrical energy generated and fan power are 45.68 W and 0.86 W, respectively. Overall, the best performance of a system can be achieved at maximum energy output with minimum pumping power.

3.4. Thermo-electro-hydraulic efficiency

Fig. 15 illustrates that the thermo and electrohydraulic efficiencies versus Re for different jet configurations at 900 W/m^2 900 W/m^2 was chosen for the optimum solar irradiance in this research according to the monthly peaks daily total direct normal irradiance in Malaysia [38]. The graph shows an increasing trend for

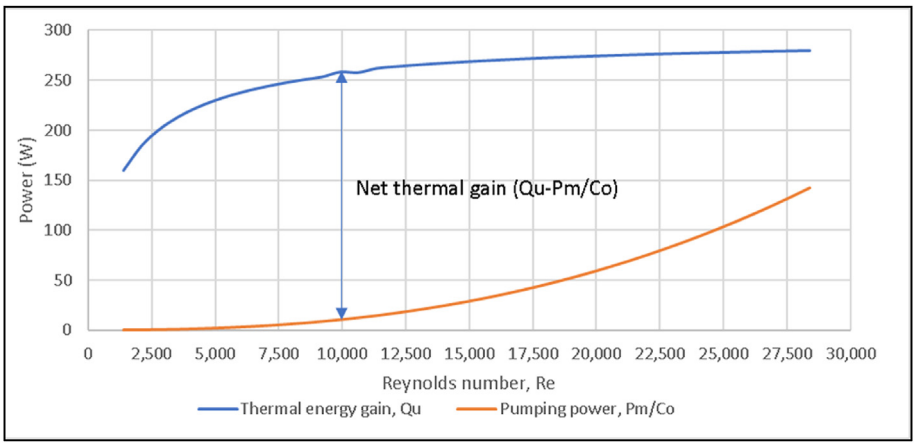

Fig. 13. Effects of Reynolds number on thermal energy gain and pumping power.

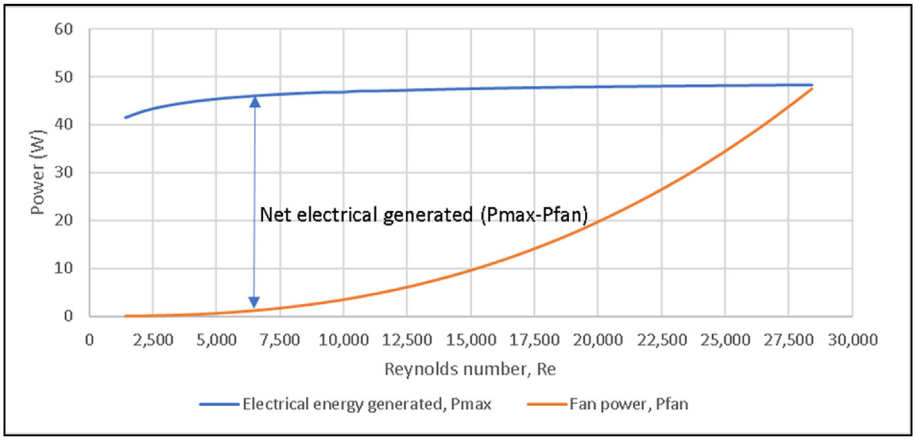

Fig. 14. Effects of Reynolds number on electrical energy generated and fan power.

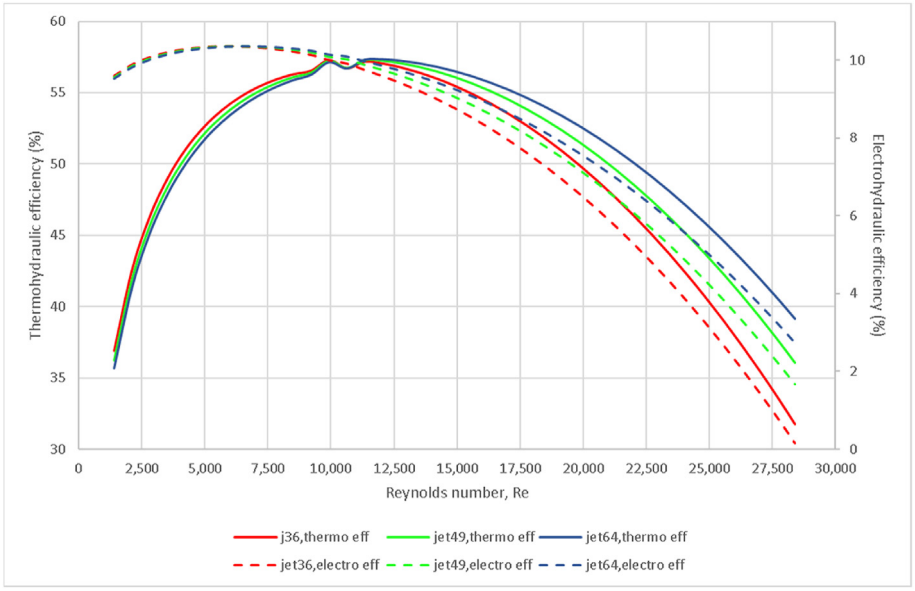

Fig. 15. Thermo and electrohydraulic efficiencies versus Re at 900 W/m.^{2}.

Table 5
Critical values of Reynolds number at which thermo and electrohydraulic efficiencies attains maxima.

Jet spacing between jet holes	Re	Max n_{thermo} achieved (%)	Re	Max $n_{electro}$ achieved (%)
X = 0.126 m; Y = 0.1134 m	9929	57.30	5667	10.36
X = 0.105 m; Y = 0.0945 m	11350	57.31	6378	10.36
X = 0.09 m; Y = 0.081 m	12060	57.36	6378	10.37

both efficiencies when the Re increases until a maximum point and decreases afterward. Thermo and electrohydraulic efficiencies are directly proportional to net thermal energy gain and net electrical energy generated. The graph shows that the maximum values for the efficiencies falls at the turbulent region, Re > 6000. When the max efficiencies drop to zero, the pumping power is equal to the energy gain, which results in zero net energy gain.

Higher efficiencies are observed at the biggest jet spacing between jet holes and the max efficiencies achieved at the laminar region. After the maximum point, the smallest jet spacing shows higher efficiencies, which is at turbulent region. This is due to the larger jet spacing between jet holes contributing to less interference, higher heat transfer, higher friction, and higher pumping power. Hence, the results reveal that the net energy gain of the largest jet spacing between jet holes is highest before the maximum point and lowest after a maximum point. The ranges of thermohydraulic efficiency for JIBPVT with 36, 49, and 64 jet-holes are 31.74–57.30%, 36.08–57.31%, and 35.70–57.36%, respectively. The ranges of electrohydraulic efficiency are 0.16–10.36%, 1.66–10.36%, and 2.74–10.37%, respectively, for jet-holes 36, 49 and 64. Table 5 listed the critical values for Re where the max efficiencies are achieved for different jet spacing between jet holes. Only a tiny variation in max efficiencies for thermo and electrohydraulic of the system between different jet spacing. Hence, the system's best performance can be explained by the lowest Re to generate max efficiencies. The critical values of Re for jet 36 are 9929 and 5667; 11350 and 6378 for jet 49; and 12060 and 6378 for jet 64. Hence, it is proved that the JIBPVT with the largest jet spacing between jet holes has the best performance.

3.5. Comparison of energy and thermo-electro-hydraulic efficiencies

Fig. 16 illustrates the energy and thermo-electro-hydraulic efficiencies for JIBPVT with 36 holes jet plate reflector. Energy efficiencies show steady increasing curves with increasing Re, while thermo and electrohydraulic efficiencies increase curves until a maximum point and decrease afterward. The frictional losses and pumping power are not considered in the calculation of energy efficiencies. Hence the curve will keep rising non-stop with increasing air velocity. Hence, to evaluate a solar system's performance with active convective heat transfer by external mechanical power, thermo-electro-hydraulic efficiencies should be prioritized instead of conventional energy efficiencies. The highest thermo,

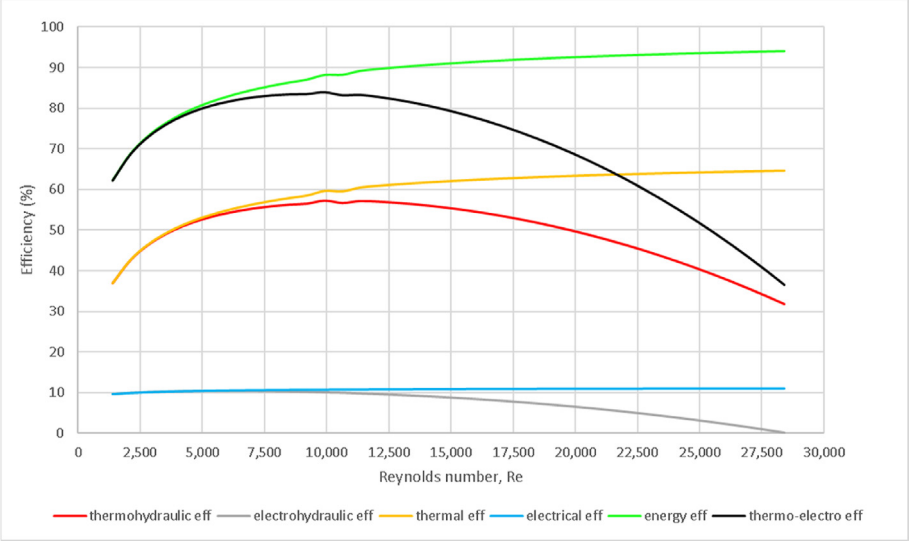

Fig. 16. Comparison of energy and thermo-electro-hydraulic efficiencies.

Table 6
Comparison of total thermo-electro-hydraulic efficiency from previous studies.

Types of solar collector	η (%)	References
JIBPVT air collector	83.9	Present Study
Jet-impingement SAC with transverse ribs absorber plate	78	[39]
Double-pass jet impingement SAC with arc roughness absorber plate	77	[40]
Bifacial PVT air collector with semi-mirror reflector	67	[23]
Jet impingement SAC with longitudinal fins absorber plate	61	[41]
Bifacial PVT double-pass air collector with mirror reflector	57	[22]
PVT with air jet	55	[18]

electro, and thermo-electro-hydraulic efficiencies of JIBPVT are 57.3%, 10.36%, and 83.93%. The lowest thermo, electro, and thermo-electro-hydraulic efficiencies are 31.74%, 0.16%, and 36.46%, respectively. Table 6 compares the energy efficiencies found in the current work and in the prior literature. The JIBPVT outperformed other air-based PVT systems, with an efficiency of 83.93%. As a result, the proposed system is a very efficient solar collector.

4. Conclusion

This study conducted thermo-electro-hydraulic analysis which had taken friction factor, pressure drop, pumping power, fan power to calculate the efficiencies. A one-dimensional heat flow analytical model in steady-state was developed to determine the energy balance between each component of the system. The simulation results were validated with experimental results and a good agreement was shown between them. The effects of packing factors of bifacial PV modules, geometric configurations of jet plate reflectors, mass flow rate, solar irradiance and other operating parameters on the performance were studied and discussed.

The following are the study's key findings:

(i) A novel design of bifacial photovoltaic/thermal solar air collector with jet impingement was presented with dual-functional jet plate reflectors.
(ii) Higher Reynolds number induced lower friction and higher pressure drop. The friction factor and pressure drop are in the range of 0.2 to 0.03 and 1.3–144.45 Pa, when Re increases from 1409 to 28404.
(iii) Increasing jet spacing between jet holes will contribute to less interference and higher heat transfer, at the same time higher friction and higher pumping power.
(iv) JIBPVT with 36 jet-holes achieved the maximum thermal energy gain and electrical energy generated at lowest Re, which are 9929 and 5667, respectively. The optimum thermal gain, pumping power, electrical energy generated and fan power are 258.31 W, 10.33 W, 45.68 W and 0.86 W, respectively.
(v) The optimum thermo, electro, and thermo-electro-hydraulic efficiencies of JIBPVT are 57.3%, 10.36%, and 83.93%.

Overall, JIBPVT, with the largest jet spacing between jet holes, has the best performance. A comparison of JIBPVT's energy efficiency with that of earlier research was also made. The JIBPVT outperformed other air-based PVT systems, with an efficiency of 83.9%. As a result, the proposed system is a very efficient solar collector.

Author statement

All the authors have equal contribution in preparation of the manuscript. The first author have original idea, Conceptualization and Methodology. The first and second authors did the data Formal analysis and Validation. The second, third and fourth authors contributed in substantial revision, editing, review and improvement of the first draft of the manuscript. Fifth, sixth and seventh authors did organization of the manuscript including language corrections and Formal analysis. In addition, Ahmad Fudholi is the main contributor in this study.

Declaration of competing interest

The authors declare that they have no known competing financial interests or personal relationships that could have appeared to influence the work reported in this paper.

Acknowledgments

The authors would like to thank UKM for its funding (GUP-2018-128).

References

[1] Geng Y, Ji W, Wang Z, Lin B, Zhu Y. A review of operating performance in green buildings: energy use, indoor environmental quality and occupant satisfaction. Energy Build 2019;183:500–14. https://doi.org/10.1016/j.enbuild.2018.11.017.
[2] gang Hwang B, Shan M, Supa'at NNB. Green commercial building projects in Singapore: critical risk factors and mitigation measures. Sustain Cities Soc 2017;30:237–47. https://doi.org/10.1016/j.scs.2017.01.020.
[3] Hwang BG, Shan M, Xie S, Chi S. Investigating residents' perceptions of green retrofit program in mature residential estatesThe case of Singapore. Habitat Int 2017;63:103–12. https://doi.org/10.1016/j.habitatint.2017.03.015.
[4] Vinet L, Zhedanov A. A 'missing' family of classical orthogonal polynomials. J Phys Math Theor 2011;44(8):32. https://doi.org/10.1088/1751-8113/44/8/085201.
[5] Houghton A, Castillo-Salgado C. Analysis of correlations between neighborhood-level vulnerability to climate change and protective green building design strategies: a spatial and ecological analysis. Build Environ 2020;168:106523. https://doi.org/10.1016/j.buildenv.2019.106523.
[6] Sansaniwal SK, Sharma V, Mathur J. Energy and exergy analyses of various typical solar energy applications: a comprehensive review. Renew Sustain Energy Rev 2018;82(May):1576–601. https://doi.org/10.1016/j.rser.2017.07.003.
[7] Pawar RS, Takwale MG, Bhide VG. Evaluation of the performance of the solar air heater. Energy Convers Manag 1994;35(8):699–708. https://doi.org/10.1016/0196-8904(94)90054-X.
[8] Forson FK, Nazha MAA, Rajakaruna H. Experimental and simulation studies on a single pass, double duct solar air heater. Energy Convers Manag 2003;44(8):1209–27. https://doi.org/10.1016/S0196-8904(02)00139-5.
[9] Choudhury C, Garg HP. Evaluation of a jet plate solar air heater. Sol Energy 1991;46(4):199–209. https://doi.org/10.1016/0038-092X(91)90064-4.
[10] Belusko M, Saman W, Bruno F. Performance of jet impingement in unglazed air collectors. Sol Energy 2008;82(5):389–98. https://doi.org/10.1016/j.solener.2007.10.005.
[11] Chauhan R, Thakur NS. Heat transfer and friction factor correlations for impinging jet solar air heater. Exp Therm Fluid Sci 2013;44:760–7. https://doi.org/10.1016/j.expthermflusci.2012.09.019.
[12] Chauhan R, Thakur NS. Investigation of the thermohydraulic performance of impinging jet solar air heater. Energy 2014;68:255–61. https://doi.org/10.1016/j.energy.2014.02.059.
[13] Chauhan R, Singh T, Thakur NS, Patnaik A. Optimization of parameters in solar thermal collector provided with impinging air jets based upon preference selection index method. Renew Energy 2016;99:118–26. https://doi.org/10.1016/j.renene.2016.06.046.
[14] Chan HY, Vinson AA, Baljit SSS, Ruslan MH. Comparison of thermal performances between low porosity perforate plate and flat plate solar air collector. J. Phys. Conf. Ser. 2018;989(1). https://doi.org/10.1088/1742-6596/989/1/012001.
[15] Matheswaran MM, Arjunan TV, Somasundaram D. Analytical investigation of solar air heater with jet impingement using energy and exergy analysis. Sol Energy 2018;161(October 2017):25–37. https://doi.org/10.1016/j.solener.2017.12.036.
[16] Chow TT. A review on photovoltaic/thermal hybrid solar technology. Appl Energy 2010;87(2):365–79. https://doi.org/10.1016/j.apenergy.2009.06.037.
[17] Takashima T, Tanaka T, Doi T, Kamoshida J, Tani T, Horigome T. New proposal for photovoltaic-thermal solar energy utilization method. Sol Energy 1994;52(3):241–5. https://doi.org/10.1016/0038-092X(94)90490-1.
[18] Brideau SA, Collins MR. Development and validation of a hybrid PV/Thermal air based collector model with impinging jets. Sol Energy 2014;102:234–46. https://doi.org/10.1016/j.solener.2014.01.022.
[19] Hasan HA, Sopian K, Jaaz AH, Al-Shamani AN. Experimental investigation of jet array nanofluids impingement in photovoltaic/thermal collector. Sol Energy 2017;144:321–34. https://doi.org/10.1016/j.solener.2017.01.036.

[20] Hasan HA, Sopian K, Fudholi A. Photovoltaic thermal solar water collector designed with a jet collision system. Energy 2018;161:412–24. https://doi.org/10.1016/j.energy.2018.07.141.
[21] Sun X, Khan MR, Deline C, Alam MA. Optimization and performance of bifacial solar modules: a global perspective. Appl Energy 2018;212(1):1601–10. https://doi.org/10.1016/j.apenergy.2017.12.041.
[22] Mustapha M, Fudholi A, Sopian K. Mathematical modelling of bifacial photovoltaic-thermal (BPVT) collector with mirror reflector. Int J Renew Energy Resour 2020;10(2):654–62.
[23] Ooshaksaraei P, Sopian K, Zaidi SH, Zulkifli R. Performance of four air-based photovoltaic thermal collectors configurations with bifacial solar cells. Renew Energy 2017;102:279–93. https://doi.org/10.1016/j.renene.2016.10.043.
[24] Zuckerman N, Lior N. Jet impingement heat transfer: physics, correlations, and numerical modeling, vol. 39. C. Elsevier Masson SAS; 2006. https://doi.org/10.1016/S0065-2717(06)39006-5.
[25] Kim JH, Park SH, Kim JT. Experimental performance of a photovoltaic-thermal air collector. Energy Proc 2014;48:888–94. https://doi.org/10.1016/j.egypro.2014.02.102.
[26] Duffie JA, Beckman WA, McGowan J. Solar Eng Therm Process 1985;53(4). https://doi.org/10.1119/1.14178.
[27] Ong KS. Thermal performance of solar air heaters: mathematical model and solution procedure. Sol Energy 1995;55(2):93–109. https://doi.org/10.1016/0038-092X(95)00021-I.
[28] Mohelníková J, Altan H. Evaluation of optical and thermal properties of window glazing. WSEAS Trans Environ Dev 2009;5(1):86–93.
[29] Cortés A, Piacentini R. Improvement of the efficiency of a bare solar collector by means of turbulence promoters. Appl Energy 1990;36(4):253–61. https://doi.org/10.1016/0306-2619(90)90001-T.
[30] Karwa R, Garg SN, Arya AK. Thermo-hydraulic performance of a solar air heater with n-subcollectors in series and parallel configuration. Energy 2002;27(9):807–12. https://doi.org/10.1016/S0360-5442(02)00016-6.
[31] Karwa R, Chauhan K. Performance evaluation of solar air heaters having v-down discrete rib roughness on the absorber plate. Energy 2010;35(1):398–409. https://doi.org/10.1016/j.energy.2009.10.007.
[32] Saini SK, Saini RP. Development of correlations for Nusselt number and friction factor for solar air heater with roughened duct having arc-shaped wire as artificial roughness. Sol Energy 2008;82(12):1118–30. https://doi.org/10.1016/j.solener.2008.05.010.
[33] Hegazy AA. Comparative study of the performances of four photovoltaic/thermal solar air collectors. Energy Convers Manag 2000;41(8):861–81. https://doi.org/10.1016/S0196-8904(99)00136-3.
[34] Fudholi A, Sopian K, Othman MY, Ruslan MH, Bakhtyar B. Energy analysis and improvement potential of finned double-pass solar collector. Energy Convers Manag 2013;75:234–40. https://doi.org/10.1016/j.enconman.2013.06.021.
[35] Fudholi A, Sopian K, Ruslan MH, Othman MY. Performance and cost benefits analysis of double-pass solar collector with and without fins. Energy Convers Manag 2013;76:8–19. https://doi.org/10.1016/j.enconman.2013.07.015.
[36] Mathioulakis E, Voropoulos K, Belessiotis V. Assessment of uncertainty in solar collector modeling and testing. Sol Energy 1999;66(5):337–47. https://doi.org/10.1016/S0038-092X(99)00034-1.
[37] Sabatelli V, Marano D, Braccio G, Sharma VK. Efficiency test of solar collectors: uncertainty in the estimation of regression parameters and sensitivity analysis. Energy Convers Manag 2002;43(17):2287–95. https://doi.org/10.1016/S0196-8904(01)00180-7.
[38] Mohammad ST, Al-Kayiem HH, Aurybi MA, Khlief AK. Measurement of global and direct normal solar energy radiation in Seri Iskandar and comparison with other cities of Malaysia. Case Stud Therm Eng 2020;18(October 2019):100591. https://doi.org/10.1016/j.csite.2020.100591.
[39] Moshery R, Chai TY, Sopian K, Fudholi A, Al-Waeli AHA. Thermal performance of jet-impingement solar air heater with transverse ribs absorber plate. Sol Energy 2021;214(November 2020):355–66. https://doi.org/10.1016/j.solener.2020.11.059.
[40] Matheswaran MM, Arjunan TV, Somasundaram D. Analytical investigation of exergetic performance on jet impingement solar air heater with multiple arc protrusion obstacles. J Therm Anal Calorim 2019;137(1):253–66. https://doi.org/10.1007/s10973-018-7926-z.
[41] Goel AK, Singh SN. Performance studies of a jet plate solar air heater with longitudinal fins. Int J Ambient Energy 2019;40(2):119–27. https://doi.org/10.1080/01430750.2017.1372808.

Nomenclature

Abbreviation and Acronyms

A_c: the total surface area of the collector (m^2)
C_p: specific heat of the air (J/(kg. K))
d: duct depth of air channel (m)
D_h: the hydraulic diameter of the air channel (m)
D_j: the diameter of jet holes (m)
h_c: convective heat transfer coefficient (W/m^2 K)
h_r: radiative heat transfer coefficient (W/m^2 K)
h_w: convective heat transfer coefficient due to wind (W/m^2 K)
I: solar irradiance (W/m^2)
k: thermal conductivity (W/(m·K))
$\dot{m}$: air mass flow (kg/s)
N: number of jet holes
N_t: the thickness of the jet plate reflector
Nu: Nusselt number
P: packing factor of PV cell
P_{max}: electrical power generated
Q_u: useful heat gain (W)
Re: Reynolds number
T: temperature (K)
U_b: bottom loss coefficient (W/m^2 K)
V_w: wind velocity (m/s)
X: streamwise pitch (m)
Y: spanwise pitch (m)
ε: emissivity
α: absorptivity
τ: transmissivity
μ: air viscosity (kg/ms)
ρ: air density (kg/m^3)
$\eta_{PVfront}$: the efficiency of the upper part of PV
η_{PVrear}: the efficiency of the rear part of PV
η_R the reflectivity of the jet plate reflector
$\eta_{thermal}$: thermal efficiency
η_{pv}: electrical efficiency of PV cell
η_{panel}: electrical efficiency of PV panel
η_{total}: total efficiency ($\eta_{\text{thermal}} + \eta_{\text{panel}}$)

Subscripts

1: air channel between jet plate and backplate
2: air channel between PV panel and jet plate
a: ambient
b: backplate
i: inlet
j: jet plate reflector
l: laminate
o: outlet.